Ambidextrous helical nanotubes from self-assembly of designed helical hairpin motifs

Spencer A. Hughes[a], Fengbin Wang[b], Shengyuan Wang[a], Mark A. B. Kreutzberger[b], Tomasz Osinski[b], Albina Orlova[b], Joseph S. Wall[c], Xiaobing Zuo[d], Edward H. Egelman[b], and Vincent P. Conticello[a,1]

[a]Department of Chemistry, Emory University, Atlanta, GA 30322; [b]Department of Biochemistry and Molecular Genetics, University of Virginia, Charlottesville, VA 22908; [c]Department of Biology, Brookhaven National Laboratory, Upton, NY 11973; and [d]X-Ray Science Division, Argonne National Laboratory, Argonne, IL 60439

Edited by William F. DeGrado, University of California, San Francisco, CA, and approved June 11, 2019 (received for review March 6, 2019)

Tandem repeat proteins exhibit native designability and represent potentially useful scaffolds for the construction of synthetic biomimetic assemblies. We have designed 2 synthetic peptides, HEAT_R1 and LRV_M3Δ1, based on the consensus sequences of single repeats of thermophilic HEAT (PBS_HEAT) and Leucine-Rich Variant (LRV) structural motifs, respectively. Self-assembly of the peptides afforded high-aspect ratio helical nanotubes. Cryo-electron microscopy with direct electron detection was employed to analyze the structures of the solvated filaments. The 3D reconstructions from the cryo-EM maps led to atomic models for the HEAT_R1 and LRV_M3Δ1 filaments at resolutions of 6.0 and 4.4 Å, respectively. Surprisingly, despite sequence similarity at the lateral packing interface, HEAT_R1 and LRV_M3Δ1 filaments adopt the opposite helical hand and differ significantly in helical geometry, while retaining a local conformation similar to previously characterized repeat proteins of the same class. The differences in the 2 filaments could be rationalized on the basis of differences in cohesive interactions at the lateral and axial interfaces. These structural data reinforce previous observations regarding the structural plasticity of helical protein assemblies and the need for high-resolution structural analysis. Despite these observations, the native designability of tandem repeat proteins offers the opportunity to engineer novel helical nanotubes. Moreover, the resultant nanotubes have independently addressable and chemically distinguishable interior and exterior surfaces that would facilitate applications in selective recognition, transport, and release.

tandem repeat proteins | cryo-EM | helical nanotube | self-assembly

Self-assembly is a ubiquitous process in biological systems. The functional macromolecular machines of living organisms commonly arise from homomeric or heteromeric self-association that involves selective recognition at the intermolecular interfaces between protomers (i.e., structural subunits). The most structurally economical method of constructing such assemblies is based on the application of a helical symmetry operation (1, 2). Helical protein assemblies encompass a diversity of functional roles in biological systems that would be desirable to emulate in synthetic or semisynthetic analogs, including controlled release and delivery (filamentous phage and viruses) (3–5) cargo transport (conjugative pili, type 3 secretion system needle complex) (6, 7), locomotion (flagellum) (8, 9), and signal transduction and actuation (pyrin domains and sterile α-motifs associated with the inflammasome and the signalosome, respectively) (10, 11), among other functions. We describe herein an approach to the fabrication of synthetic helical protein nanotubes derived from tandem repeat proteins (TRPs) based on helical hairpin structural motifs. These helical assemblies represent promising substrates for the construction of synthetic compartments with structural and, potentially, functional asymmetry since the interior (concave) and exterior (convex) surfaces can be structurally distinguished based on the mode of self-association of the protomers. The resultant assemblies approximate the dimensions and helical architecture of native protein and nucleoprotein filaments, which offers the opportunity to engineer synthetic peptide-based nanomaterials that display a range of functional roles similar to those of the corresponding biological assemblies.

The design of helical nanotubes depends on the ability to control the noncovalent interactions between protomers that drive self-assembly. Helical assemblies are usually characterized in terms of the number of subunits per helical turn, N (= $2\pi/\phi$); the helical pitch, P (= Nz); and the helical radius, r, in which ϕ and z refer to the twist angle and axial rise, respectively. In the simplest cases, these parameters can be determined from assignment of a one-start helix, i.e., a helix that passes through every subunit in the structure. These assemblies need not form closed cylinders, i.e., structures in which successive turns of the helical assembly make stable physical contacts through an axial interface. However, the corresponding tubular structures may be the most suitable targets for construction of asymmetric interfaces, that is, those in which the external and internal surfaces of the assembly can be structurally distinguished and functionally addressed. Helical protein nanotubes result from cohesive lateral and axial self-association of protomers into a hollow cylinder in which a central channel (lumen) runs through the structure and

Significance

The helical structures of biological filaments provide inspiration for the creation of synthetic analogues, which, unconstrained by evolution, may be designed to perform unique functions under conditions that differ from the native cellular environment. However, the structural polymorphism of helical assemblies represents a significant challenge to the predictable and controllable self-assembly of synthetic peptide filaments. Herein, we identify 2 natively designable helical hairpin motifs as a basis for the rational design of peptide nanotubes that capture structural features of native protein filaments, including helical supramolecular architecture, high aspect ratio, and structurally distinguishable concave and convex surfaces. Atomic models, generated from three-dimensional reconstruction of cryo-EM images, confirm the preservation of local structural interactions, although the helical architecture differs from prediction.

Author contributions: S.A.H. and V.P.C. designed research; S.A.H., F.W., S.W., M.A.B.K., A.O., J.S.W., X.Z., and E.H.E. performed research; S.A.H., F.W., S.W., M.A.B.K., T.O., J.S.W., X.Z., E.H.E., and V.P.C. analyzed data; and S.A.H., F.W., S.W., M.A.B.K., T.O., A.O., J.S.W., X.Z., E.H.E., and V.P.C. wrote the paper.

The authors declare no conflict of interest.

This article is a PNAS Direct Submission.

Data deposition: The atomic coordinates and structure factors have been deposited in the Protein Data Bank, https://www.wwpdb.org/ (PDB ID codes 6MK1 and 6HQE), and the Electron Microscopy Data Bank (accession codes EMD-9136 and EMD-0252).

[1]To whom correspondence may be addressed. Email: vcontic@emory.edu.

This article contains supporting information online at www.pnas.org/lookup/suppl/doi:10.1073/pnas.1903910116/-/DCSupplemental.

Published online July 1, 2019.

is oriented parallel to the helical axis. Considerable structural evidence suggests that the quaternary structure of helical protein assemblies may not be robust in sequence space and, therefore, may be limited in designability (12–22). The potential plasticity of quaternary structure in sequence space represents a significant challenge to the rational design of helical nanotubes. One approach to avoid this bottleneck may be to identify peptide or protein motifs that correspond to quaternary structures that are natively designable.

TRPs (23) constitute a diverse and highly designable protein supergroup (24–26) that shows considerable promise for fabrication of robust supramolecular scaffolds. TRPs comprise repetitive domains in which structural motifs of 20 to 50 amino acids are concatenated with varying levels of sequence identity that depend on the repeat protein family (23, 27). Consensus repeats have been defined for a number of solenoidal TRPs, including tetratricopeptide repeat (TPR) (28); ankyrin (29); armadillo (30); Huntingtin, Elongation Factor 3, Protein Phosphatase Subunit A, and Yeast Kinase Tor1 (HEAT) (31); and leucine-rich (LRR) repeats (32). Synthetic solenoidal repeat proteins derived from consensus sequences display structures that mimic the 3D structures of the respective native TRPs. Moreover, computational methods have been employed for the de novo design of a diverse range of synthetic TRPs (23, 33–36). In these cases, good agreement was observed between the crystallographically determined structures and the corresponding computational models for a number of TRPs based on different repeat motifs. Most native solenoid proteins form open and extended supramolecular structures with strong lateral interactions but negligible axial interactions between successive helical turns. In addition, native TRPs are often capped at the N and C termini to prevent uncontrolled noncovalent polymerization, which is usually an unwanted outcome from the perspective of biological function. Therefore, native TRP sequences are not necessarily amenable as substrates for the construction of synthetic helical nanotubes. Recently, Shen et al. (37) reported the computational design of self-assembling filaments from self-assembly of synthetic TRPs with excellent agreement between the computational models and the cryo-electron microscopy (cryo-EM)–derived structures. This study treated the TRPs as generic building blocks in which the local symmetry of the repeat was not continuously maintained throughout the structure. However, we have identified 2 related classes of TRP motifs based on helical hairpin structures derived from leucine-rich repeat variant (LRV) (38) and phycobilisome lyase HEAT-like (PBS_HEAT) (39) that may be capable of forming closed cylindrical assemblies. We report the design, synthesis, and structural characterization of 2 peptide sequences, **LRV_M3Δ1** and **HEAT_R1**, based on these motifs that self-assemble into structurally robust, thermally stable helical nanotubes, in which the local cohesive interactions between protomers corresponding to 1 or 2 repeat motifs are maintained throughout the assembly.

Rees and coworkers (38) first described the LRV repeat motif in 1996 from the crystallographic analysis of a protein (Protein Data Bank [PDB] ID 1LRV) derived from a cryptic open-reading frame in the nitrogen-fixing bacterium *Azotobacter vinelandii* (Fig. 1). The structure of the protein comprised 2 domains: an Fe_4–S_4 cluster protein and a series of 8 helical repeats of 24 amino acid residues described as concatemers of an LRV domain. The LRV repeat motif (Pfam database, PF01816) is based on a 3_{10} helix–loop–alpha helix structure, in which the 3_{10} helix lies at the exterior (convex) surface and the α helix lies at the interior (concave) surface. The structure of the LRV repeat sequence in 1LRV corresponds to a right-handed superhelix with an average twist angle between successive repeat motifs of ∼15°. Remarkably, Rees and coworkers predicted on the basis of this crystal structure that the LRV domain could potentially form a helical nanotube with a pitch of 32 Å and ∼24 subunits per turn of the superhelix. Subsequently, Minard and coworkers (39) described a class of HEAT repeat proteins, PBS_HEAT (SMART database, SM000567, and Pfam database, PF03130), derived from thermostable microbes. In contrast to the LRV motif, the PBS_HEAT repeat comprises an alpha helix–loop–alpha helix motif of 31 amino acids. They defined a consensus repeat sequence for the PBS_HEAT motif and synthesized and characterized a series of concatemers based on this sequence. The inner (concave) helix of the consensus sequence displays similarity to the α helix of the LRV repeat in that specific residues that mediate interactions at the lateral interface are conserved between the 2 sequences (Fig. 1*A*). They reported the crystal structure of a tetramer of the consensus HEAT repeat sequence, αRep-n4-a (PDB ID 3LTJ), which displayed a right-handed helical curvature with an average angle of

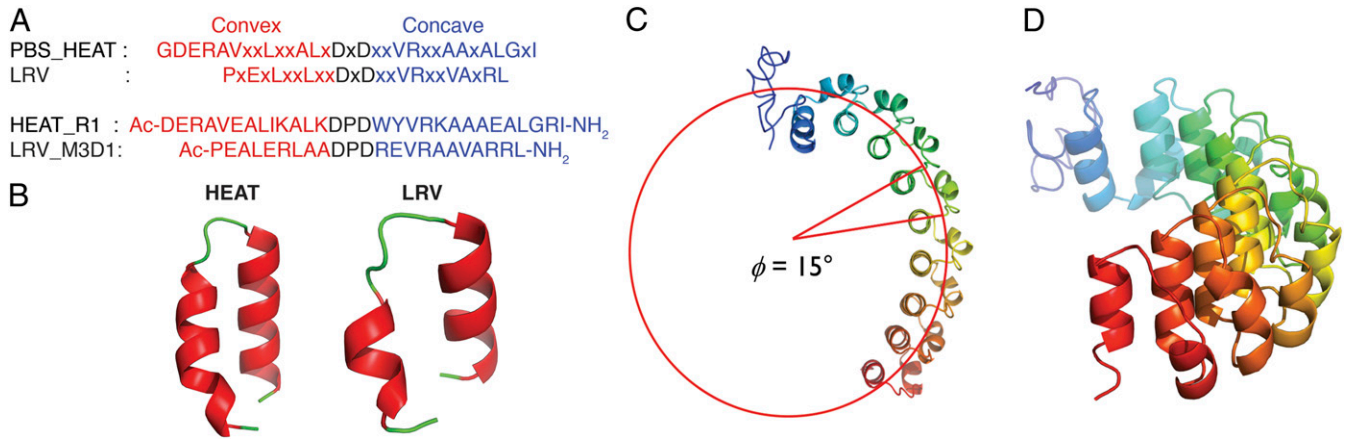

Fig. 1. Design of synthetic helical nanotubes from tandem repeat peptide sequences. (*A*) Conserved sequence positions for the PBS_HEAT and LRV repeat motifs and the corresponding sequences of the synthetic peptides **HEAT_R1** and **LRV_M3Δ1**. The sequence features corresponding to structural motifs located at the convex and concave surfaces are colored red and blue, respectively. Conserved and semiconserved residues between the PBS_HEAT and LRV repeat sequences are depicted in bold and are located at the turn and concave helix. (*B*) Structures of representative repeat units from the crystal structures of 3LTJ and 1LRV. Concave helices are depicted on the right side of the respective images. (*C*) Top view of the crystal structure (PDB ID 1LRV) of *A. vinelandii* protein (GenBank accession no. M20568) comprising an N-terminal Fe_4S_4 cluster protein domain (line diagram in blue) fused to a series of 8 LRV domains. Successive LRV repeat motifs undergo an average rotation through a twist angle of circa 15° with respect to a central axis that is perpendicular to the plane of the image. (*D*) Side view of the crystal structure of the same protein in which the right-handed helical curvature of the LRV concatemer can be discerned.

20° between successive repeat motifs. These results suggest that the mode of subunit packing in the folded concatemer is similar between the LRV and PBS_HEAT repeat motifs, although the internal rotational angle—analogous to the twist angle, ϕ, of a helical assembly—differs between the 2 structures.

Results

Peptide Design and Synthesis. Two peptide sequences, **HEAT_R1** and **LRV_M3Δ1**, were designed from the consensus sequences of the PBS_HEAT and LRV repeat motifs, respectively (Fig. 1*B*). The N-terminal amino acid was deleted from the respective consensus sequences and replaced with a smaller acetyl group to prevent steric interference between the termini of successive protomers in the helical assembly. The identities of charged groups at surface exposed sites were chosen to minimize repulsive electrostatic interactions and maintain the pI of the resultant peptides within the near-neutral pH range. Highly conserved residues within the respective repeat sequences were maintained in the synthetic peptides as these positions mediated structurally critical lateral interactions between protomers in the respective TRPs. The design of each peptide was derived from a single repeat unit of the LRV and PBS_HEAT motifs based on the following considerations: ease of synthesis of traceless (i.e., tag-free) sequences, removal of additional turn sequences between concatenated repeat motifs that could inhibit axial stacking interactions, and the greater conformational freedom of short peptide sequences that may more easily accommodate the formation of large assemblies. The disadvantage of this approach is that single repeat motifs may not adopt a thermodynamically stable conformation corresponding to the native fold. Modeling of the folding of TRPs derived from consensus TPR and ankyrin motifs suggested that the stability of the corresponding repeat proteins was related to the number of repeat units and the strength of lateral association (40–42). Individual subunits of consensus repeats may be poised on the edge of instability but still appear stable at 25 °C. Minard and coworkers (39) described the thermal denaturation of a series of concatemers of thermostable PBS_HEAT consensus repeats (n = 1, 2, 3, 4, and 6) cloned between optimized N-terminal and C-terminal capping sequences. The T_m value of the monomer, αRep-n1-a, was determined to be ∼71–72 °C in dilute aqueous solution (100 μM protein, 50 mM phosphate buffer, pH 7). While the monomer actually consisted of 3 repeats due to the presence of the capping motifs, these data demonstrated that individual repeat motifs might be sufficiently stable at ambient temperature.

Peptides **HEAT_R1** and **LRV_M3Δ1** were prepared using microwave-assisted solid-phase synthesis and purified via reverse-phase HPLC. The purity and identity of the corresponding peptides were confirmed by analytical HPLC and MALDI-TOF mass spectrometry (*SI Appendix*, Figs. S1–S4). Circular dichroism (CD) spectropolarimetry was employed to interrogate the conformational behavior of the peptides in aqueous buffer. The **HEAT_R1** and **LRV_M3Δ1** peptides displayed significant differences in their respective CD spectra, which could be interpreted in terms of the relative conformational stability of the repeat motifs. The **HEAT_R1** peptide displayed a classical α-helical CD signature with a positive signal at 193 nm and negative minima at 208 and 222 nm over a range of pH values and temperature (*SI Appendix*, Figs. S5–S7). The CD spectra of **HEAT_R1** in buffered aqueous solutions strongly resemble the corresponding CD spectra of consensus PBS_HEAT repeats in the αRep series of capped concatemers reported by Minard and coworkers (39). In contrast, the CD spectra of **LRV_M3Δ1** displayed a spectroscopic response that evolved over time (*SI Appendix*, Fig. S8). A single strong minimum was initially observed at 226 nm with a shoulder at shorter wavelengths. The mature CD spectrum resembled an α-helical conformation, albeit with differences in that the minima were observed at wavelengths of 204 and 224 nm, which were shifted in position with respect to a canonical α-helical conformation (*SI Appendix*, Fig. S8). The observed CD profile could not be clearly interpreted in terms of an α helix–loop–α helix or a 3_{10} helix–loop–α helix (38). While aggregation of filamentous structures can attenuate the short-wavelength CD signal, transmission electron microscopy (TEM) imaging of the LRV assemblies did not provide evidence for higher-order association or the presence of aggregates. The LRV repeat motif is significantly shorter than the PBS_HEAT motif such that conformational plasticity of the convex helix could influence the development of the observed CD signal.

Negative-stained TEM was used to screen for self-assembly of the **HEAT_R1** and **LRV_M3Δ1** peptides and to determine the resultant morphology of the corresponding assemblies (*SI Appendix*, Fig. S9). High-aspect ratio filaments were observed from self-assembly of both peptides within the pH range from 5 to 8 in aqueous buffer. The resultant filaments seemed to be stable in solution for a period of at least several weeks at ambient temperature. The filaments were uniform in diameter but polymorphic in the length, ranging from 50 nm to 5 μm. The apparent widths of the filaments were measured to be circa 9 nm for **HEAT_R1** and **LRV_M3Δ1**. The differential contrast between the edges of the structures and the internal portion confirm the formation of nanotubes. The inner lumen appears darker in negative-stained TEM images of both classes of filaments due to infiltration of negative stain into the central channel. Despite apparent differences in peptide conformation, sequence, and length, the **HEAT_R1** and **LRV_M3Δ1** filaments displayed similar morphology. However, the absence of high-resolution structural information precluded a conclusive determination that the structures were equivalent to each other or to the helical nanotube structure initially proposed by Rees and coworkers (38).

Cryo-EM Structural Analysis. To resolve these issues, particularly in light of the aforementioned polymorphism of helical polymers assembled in vitro, the structures of the assemblies were analyzed using cryo-EM with direct electron detection (Fig. 2). The 3D reconstructions were generated using iterative helical real-space reconstruction (IHRSR). Final resolutions of 4.4 and 6.0 Å for **LRV_M3Δ1** and **HEAT_R1** filaments, respectively, were determined from the Fourier shell correlation (FSC) between the maps and the models (*SI Appendix*, Fig. S10, and Table 1). The structure of the **HEAT_R1** filaments displays a right-handed helix with a pitch of ∼31 Å and 10.3 asymmetric units per turn. Contrary to expectation, the asymmetric unit of the **HEAT_R1** assembly corresponded to a dimer of helical hairpin subunits (Fig. 2*E*) for an overall number of 20.7 peptides per helical turn, which was in approximate agreement with the estimates from the scanning transmission electron microscopy (STEM) mass-per-length measurements (*SI Appendix*, Fig. S11). The power spectrum displayed a strong peak at 31 Å corresponding to the one-start helix, which was also observed in the synchrotron small-angle X-ray scattering (SAXS) curve for aqueous solutions of **HEAT_R1** filaments at a q value of 0.20 $Å^{-1}$ (*SI Appendix*, Fig. S12).

In comparison, the structure of the **LRV_M3Δ1** filaments consisted of a left-handed helix with a pitch of 20 Å and 17.4 subunits per turn (Fig. 2*B*). Notably, the observed helical parameters for the **LRV_M3Δ1** filament differed significantly from the helical nanotube structure that Rees and coworkers (38) proposed for an assembly derived from the structure of 1LRV. Moreover, the protomer structure deduced from fitting of the EM density map was consistent with an α loop–α helical hairpin rather than the 3_{10} loop–α helical hairpin observed in the crystal structure 1LRV (*SI Appendix*, Fig. S13). The spacing of 20 Å associated with the one-start helix of the **LRV_M3Δ1** filament was not observed in the corresponding synchrotron SAXS curve (*SI Appendix*, Fig. S12). The hairpin turn of a protomer within

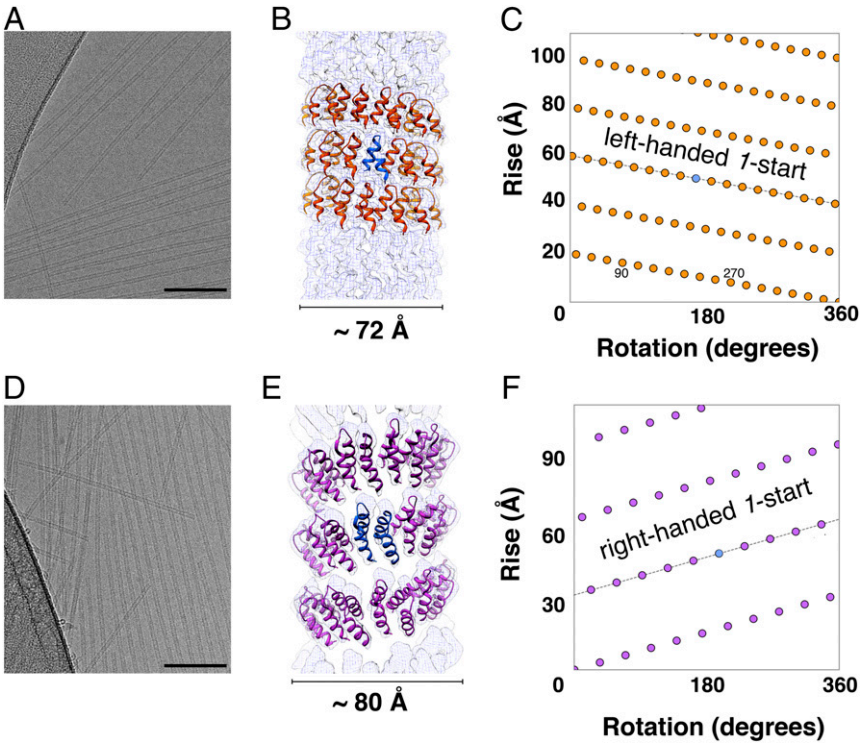

Fig. 2. (*A* and *D*) Cryo-EM images of **LRV_M3Δ1** (*A*) and **HEAT_R1** (*D*) filaments. (Scale bar, 100 nm.) (*B* and *E*) Three-dimensional reconstructions of the **LRV_M3Δ1** (*B*) and **HEAT_R1** (*E*) filaments fit with the corresponding atomic models. The asymmetric units are highlighted for the respective filaments in blue, which, in the case of **HEAT_R1**, corresponds to a dimer of peptides. (*C* and *F*) Helical nets for the **LRV_M3Δ1** (*C*) and **HEAT_R1** (*F*) filaments, in which the difference in helical hand is apparent. The helical nets show the unrolled surface lattice viewed from the outside of the filament.

the **LRV_M3Δ1** filament makes a close contact with the N and C termini of axially adjacent protomers of a successive helical turn. Protomers within the **LRV_M3Δ1** filament display a minimal tilt with respect to the central helical axis of the assembly; consequently, the filament appears at low resolution as a smooth cylinder. In contrast, protomers within the **HEAT_R1** filament are tilted away from the central helical axis of the assembly such that the concave helix at the turn surface makes contact with the N terminus of the convex helix of an axially adjacent protomer. Similarities were observed between the structures of the **HEAT_R1** and **LRV_M3Δ1** filaments in that the conserved concave α helices lined the inner lumen, as expected, with the more variable N-terminal helix located at the convex surface, as predicted for helical nanotubes based on the structures of PBS_HEAT and LRV repeat proteins.

Table 1. Refinement statistics for the peptide filament models

	HEAT_R1	LRV_M3Δ1
Helical symmetry		
Rise (Å)	3.02	1.15
Rotation (°)	34.8	−20.7
Resolution estimates (Å)		
Model:map FSC (0.143/0.38/0.5)	5.1/6.0/6.3	4.0/4.4/4.5
d_{model}	5.8	4.4
d_{99}	5.5	4.3
Model vs. data correlation coefficient	0.82	0.85
Clash score, all atoms	4.15	4.61
Protein geometry		
Ramachandran favored (%)	94.6	95.2
Ramachandran outliers (%)	0	0
Rotamer outliers (%)	0	0
Cβ deviations > 0.25 Å	0	0
RMS deviations		
Bond (Å)	0.01	0.01
Angles (°)	1.34	1.22
MolProbity score	1.69	1.57
PDB ID	6MK1	6HQE
Electron Microscopy Data Bank ID	EMD-9136	EMD-0252

Synchrotron SAXS measurements on aqueous solutions of the **HEAT_R1** and **LRV_M3Δ1** peptides confirmed the presence of uniform diameter cylindrical rods (*SI Appendix*, Fig. S12). The SAXS data for **LRV_M3Δ1** and **HEAT_R1** were fit to a modified Guinier fit for rod-like forms (*SI Appendix*, Fig. S14). The cross-sectional radius of gyration, R_c, was determined from the SAXS data for **LRV_M3Δ1** and **HEAT_R1** assemblies, which resulted in values of 30.5 ± 1.3 Å and 33.4 ± 0.6 Å, respectively. The corresponding R_c values, calculated from the atomic models derived from the 3D reconstructions, were determined to be 30.4 and 30.8 Å for the **LRV_M3Δ1** and **HEAT_R1** assemblies. The experimentally determined R_c value for the **LRV_M3Δ1** assemblies correlates well with that calculated from the atomic model resulting from the 3D reconstruction. In contrast, the R_c value determined from the SAXS data for the **HEAT_R1** assemblies is significantly larger than that calculated from the atomic model. This discrepancy may reflect the fact that weakened axial interactions between successive helical turns in the **HEAT_R1** assemblies (vide infra) result in greater flexibility. Local unwinding of the helical filaments is observed in STEM images of negatively stained specimens of the **HEAT_R1** filaments (*SI Appendix*, Fig. S15).

Discussion

The structural analyses of the **HEAT_R1** and **LRV_M3Δ1** filaments highlight the challenge of polymorphism in helical assemblies

and the difficulties associated with prediction of quaternary structure. High-resolution structural information offers the opportunity to gain insight into the features that might be responsible for the differences between the predicted and observed structures. The **HEAT_R1** filament exhibits right-handed helical twist, as was expected in analogy to the curvature observed in the crystal structures of proteins containing concatemers of LRV (PDB ID 1LRV) and PBS_HEAT (PDB ID 3LTJ) repeat motifs. However, a local break in symmetry occurs in the **HEAT_R1** structure due to an apparent interaction between tryptophan residues within the 2 chains in the asymmetric unit (Fig. 3*A*). In the structural model of the **HEAT_R1** filament, this interaction is manifested through planar π-stacking between *anti*-oriented tryptophans. Consequently, only 1 of the 2 **HEAT_R1** chains in the asymmetric unit of the filament can be aligned with the consensus PBS_HEAT repeats derived from the crystal structure of 3LTJ (*SI Appendix*, Fig. S16). The geometrical requirements of the Trp–Trp interaction cause significant deviation of the other chain from the PBS_HEAT repeat structure at the turn surface, which primarily involves a large movement of the peptide backbone and a flip of the aromatic ring to promote stacking with the corresponding side chain of a residue on the adjacent chain in the asymmetric unit. While the final resolution of the EM density map was only about 6.0 Å, the π−π stacking was adopted automatically during Phenix refinement, which suggested that the Trp–Trp interaction was energetically favorable and represented a reasonably good fit into the map.

To probe the importance of this aromatic interaction, the tryptophan residue involved in this interaction within the sequence of **HEAT_R1** was mutated to a phenylalanine (*SI Appendix*, Figs. S17 and S18). Despite the potential for a weaker interaction between protomers in the asymmetric unit, the **HEAT_R1_W17F** mutant assembled into filaments that displayed similar properties to the wild-type sequence on the basis of negative stain TEM and SAXS measurements (Fig. 3*C*). In particular, the strong diffraction peak at ∼31 Å, associated with the pitch of the one-start helix, was maintained in the SAXS scattering curve of the **HEAT_R1_W17F** filaments. In contrast, a W17A, Y18W double mutant of the **HEAT_R1** peptide, **HEAT_R1_AW**, was synthesized in which an alanine replaced the tryptophan residue involved in the π−π interaction between peptides in the asymmetric unit. **HEAT_R1_AW** assembled into filaments under conditions similar to those of **HEAT_R1**; however, extensive lateral aggregation was observed with concomitant loss of the 31 Å diffraction peak in the SAXS curve (*SI Appendix*, Figs. S19–S23). These results suggest that the aromatic interaction within the protomer stabilizes the supramolecular structure and may be associated development of the axial periodicity despite the fact that the Trp residues make only 1 close contact (within 5 Å) with an axially adjacent protomer. In the corresponding crystal structure of a more sequence-diverse PBS_HEAT tetramer, αRep-n4a (PDB ID 3LTJ) (39), a single aromatic π interaction occurs between Trp96 and Phe127 residues in adjacent repeat motifs at nearly equivalent positions near the N terminus of the concave helix (Fig. 3*B*). This interaction appears more readily accommodated within the regular geometry of the larger protein concatemer and does not result in local symmetry breaking.

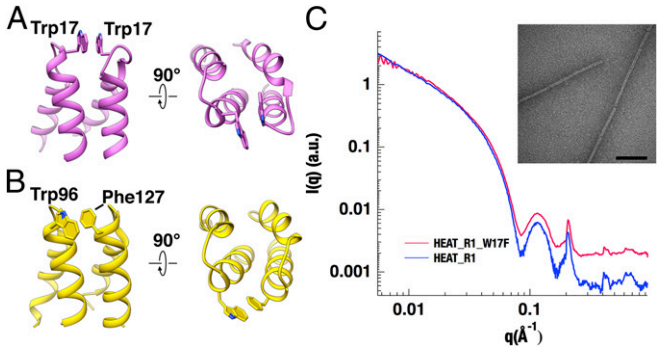

Fig. 3. (*A* and *B*) Lateral and axial views of the π-stacking interactions between protomers in the asymmetric unit of the **HEAT_R1** filament (*A*) and between 2 adjacent helical hairpin motifs ($^{79\text{-}139}$αRep-n4-a) in the crystal structure 3LTJ (*B*). (*C*) Comparison of the synchrotron SAXS scattering profiles for assemblies of the **HEAT_R1** peptide and the W17F mutant peptide (6 mg/mL in 10 mM MES buffer, pH 6.0, and 10 mM acetate buffer, pH 5.0, respectively). (*Inset*) Negative stain TEM image of filament derived from self-assembly of the **HEAT_R1_W17F** mutant peptide. (Scale bar, 100 nm.)

The importance of this aromatic interaction may be intuited indirectly through the absence of a chain of conserved hydrogen-bonded interactions between the main-chain carbonyl group and the side-chain carboxylate of Asp14 and the side-chain guanidinium group of Arg20. These residues are strongly conserved at homologous positions within the sequences of PBS_HEAT and LRV motifs (Fig. 1*A*) and mediate interactions between successive repeats. These interactions are not observed in the structure of the **HEAT_R1** filament but are preserved in the structure of the PBS_HEAT tetramer, αRep-n4-a (PDB ID 3LTJ), even in the presence of the single aromatic interaction described above. In the case of the **HEAT_R1** filament, the potential strength of the aromatic interaction between chains in the asymmetric unit may preclude the formation of these Asp–Arg interactions. The resultant structural distortion weakens the contact between protomers located at successive turns of the helix, which introduces disorder that limits the resolution to which resultant structure of **HEAT_R1** filaments can be determined. PISA (proteins, interfaces, structures, and assemblies) analysis (43) of the **HEAT_R1** filament indicated that significantly greater surface area was buried at the lateral interfaces in comparison with the axial interfaces. Due to the presence of the dimeric asymmetric unit, 2 distinct lateral and axial interfaces are observed for **HEAT_R1** repeats in the filament (Fig. 4 *B* and *E*). The 2 lateral interfaces bury 1,054 and 1,070 Å^2 of surface area, which compares well to the average of 1,124 Å^2 in buried surface area observed for lateral interactions between the consensus PBS_HEAT repeats in the crystal structure of the synthetic tetramer, 3LTJ. In contrast, the corresponding axial interfaces between protomers in the **HEAT_R1** filament bury 317 and 260 Å^2 of surface area (Fig. 4*E*). The weak axial interactions may also be responsible for local unwinding of the **HEAT_R1** filaments, which is frequently observed in EM image analysis (*SI Appendix*, Fig. S15). Similar local strand unwinding has been observed for chaperone-usher pili. Near-atomic resolution structural analysis of the corresponding pili with cryo-EM revealed that the unwinding of the helical assembly occurred analogously at the weaker axial interface (44–46).

The nature of the cohesive interactions between protomers within the **LRV_M3Δ1** filament is quite distinct from those of the **HEAT_R1** filament, especially at the axial interface. The absence of aromatic residues near the N terminus of the concave α helix for **LRV_M3Δ1** precludes local pairwise desymmetrization of adjacent subunits that would result in a structure that resembles that of the **HEAT_R1** filaments. In contrast to the **HEAT_R1** assembly, the position of the protomers in **LRV_M3Δ1** filament is consistent with maintenance of the conserved Asp–Arg interactions between adjacent subunits in the structure, although the resolution of the corresponding structure precludes a conclusive determination. Axial contacts in the **LRV_M3Δ1** filament are largely mediated through interactions between Arg13 residues and Arg22 residues within protomers located at successive turns of the helical assembly, with a contribution of Arg21 to lateral association (Fig. 4*E*). Arg13 lies on the distal side of the Asp–Pro–Asp turn sequence at the N terminus of the concave α helix,

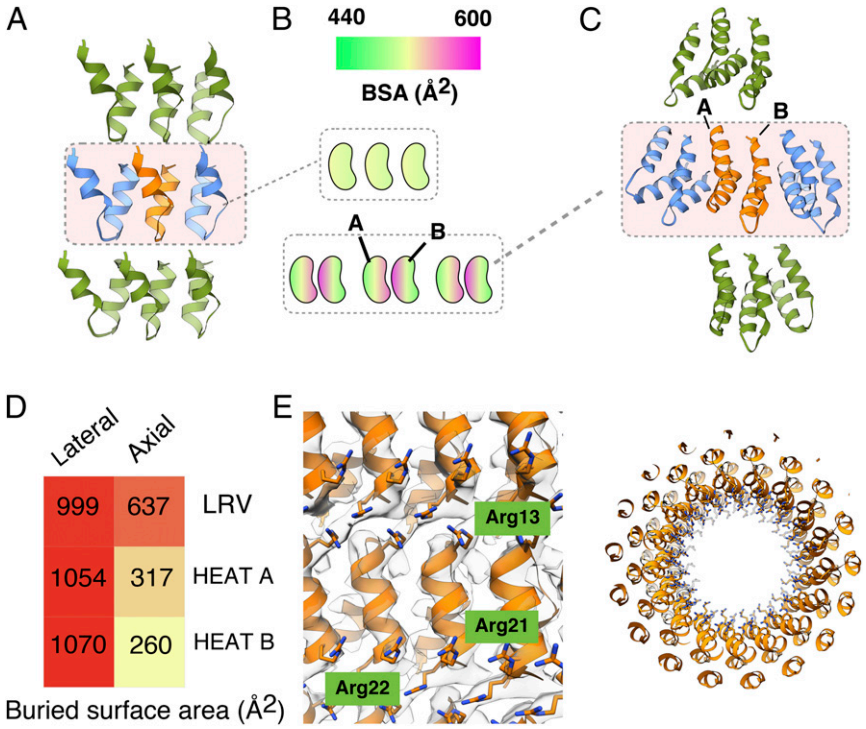

Fig. 4. HEAT map (*B*) of buried surface area determined from PISA analysis (*D*) of lateral interactions between protomers in the 3D reconstructions of the **LRV_M3Δ1** (*A*) and **HEAT_R1** (*C*) filaments. (*E*) Lateral and axial views of the 3D reconstruction of the **LRV_M3Δ1** filament in which the ordered side chains of arginine residues mediate interactions between protomers.

while Arg22 lies near the C terminus of the same helix. While Arg22 is conserved at a homologous position within the LRV domains of 1LRV, the corresponding position of Arg13 is not conserved within either LRV or PBS_HEAT motifs. These arginine residues mediate a network of noncovalent interactions that appear to be the driving force that holds together the axial interface. These axial interactions may be assisted through the preorganization of the protomers due to the strong lateral interactions that restrict the geometry of adjacent helical hairpins.

Clusters of arginines have been observed in the form of rings, ladders, and chains at the interacting interfaces between protein oligomers (47). Arginine residues, in general, appear to be overrepresented at protein–protein interfaces (48, 49). PISA analysis (43) of the **LRV_M3Δ1** filament indicates that 999 and 637 $Å^2$ of surface area is buried at the lateral and axial interfaces, respectively, between protomers. The energetics of lateral interaction for the **LRV_M3Δ1** filament compares well to the corresponding interaction between lateral interfaces within the **HEAT_R1** filament, as well as to the lateral interactions between LRV repeats in the crystal structure 1LRV (average buried surface area of 980 $Å^2$ per repeat). This lateral interaction is primarily mediated through association between concave α helices in structurally adjacent protomers as the convex helices are well separated as in the corresponding crystal structure (38). The axial interaction between **LRV_M3Δ1** protomers buries nearly twice as much surface area per subunit as the corresponding set of interactions in the **HEAT_R1** filament. This difference may account for the absence of filament unwinding and greater apparent persistence length for **LRV_M3Δ1** filaments observed in TEM images.

The left-handed helical twist observed for the **LRV_M3Δ1** filament is relatively unusual for TRPs based on helical hairpin motifs (34). Maintenance of the cohesive interactions between arginine residues at the axial interface may account for the observed differences in helical parameters for the **LRV_M3Δ1** filament from those proposed by Rees and coworkers (38) for an LRV-based nanotube. The concave helices of the LRV subunits are slightly tilted rightward with respect to the superhelical axis, and this packing geometry may influence the helical symmetry of the assembly through restricting the available modes in which the arginine residues can interact at the axial interface. Alternatively, the right-handed helical twist observed in the crystal structure of 1LRV may result from the presence of the N-terminal Fe_4–S_4 protein domain (Fig. 1 *B* and *C*), which could potentially inhibit folding of the LRV repeats with a left-handed helical twist and/or promote the formation of a right-handed helix. The attachment of a chiral endgroup has been demonstrated to induce a given helical hand in an otherwise achiral backbone to which it is attached (50). Numerous examples of this chiral domino effect have been reported for peptides and synthetic foldamers (51–53). A similar domino effect could be operative in the case of the 1LRV structure in which the presence of the terminal domain induces a diastereo-selection for the opposite helical hand. The observance of this effect would require a relatively small energy difference between the right-handed and left-handed helical conformations. Precedence for this phenomenon occurs among bacterial flagellar filaments, which can dynamically switch between different conformational states in response to mechanical forces and can be locked into specific conformations through point mutagenesis (9).

One significant question is the relevance of the nanotube structures to the corresponding structures of the TRPs that served as the starting point for the designs. In both the LRV and PBS_HEAT systems, similarities are observed between the structures of the respective protomers in the helical assemblies and in the corresponding TRPs. In addition, the lateral cohesive interactions between subunits at the concave interface are largely retained. However, significant differences are observed in the higher-order structural interactions that determine helical symmetry. The **LRV_M3Δ1** and **HEAT_R1** peptides correspond to

single repeat motifs and consequently have a greater degree of conformational freedom and, presumably, can be accommodated into a wider range of structures than repetitive proteins in which the same structural motifs are covalently linked. To assess whether the structures of the synthetic nanotubes can be preserved when the repeats are covalently linked, 2 peptides, **HEAT_dimer** and **LRV_dimer**, were synthesized (*SI Appendix*, Figs. S24–S27) in which the respective repeats were concatenated through use of turn linkages typically observed in the consensus sequences of the LRV and PBS_HEAT repeat motifs (Fig. 5*A*). The sequence of **LRV_dimer** was a direct repeat of the **LRV_M3Δ1** peptide sequence, while the sequence of **HEAT_dimer** was largely based on the sequence of **HEAT_R1** but incorporated Trp and Phe residues at positions within the sequence that were compatible with the formation of a π interaction between adjacent repeats corresponding to amino acids ^{79}Asp–^{139}Ile in the crystal structure of αRep-n4-a (Fig. 3*B*).

CD spectropolarimetric analysis of the **HEAT_dimer** peptide indicated a similar conformation in solution to the corresponding **HEAT_R1** peptides that contained a single repeat motif (*SI Appendix*, Fig. S28). In contrast, the **LRV_dimer** displayed a CD spectrum that differed from that of the **LRV_M3Δ1** filaments, primarily in that the shorter wavelength signal was significantly more intense than that at longer wavelength. Such differences in helical dichroism have been attributed to the presence of 3_{10} helix (54). Significant differences were observed in self-assembly behavior between the **HEAT_dimer** and **LRV_dimer** peptides. TEM imaging of the LRV_dimer indicated the presence of high-aspect ratio filaments of similar apparent diameter (circa 9 nm) to those observed under corresponding conditions for the **LRV_M3Δ1** peptide (Fig. 5). The formation of filamentous assemblies of **LRV_dimer** was additionally confirmed from the SAXS scattering profile (*SI Appendix*, Fig. S29). In contrast, the **HEAT_dimer** formed ill-defined aggregates under a range of conditions in aqueous buffered solution (*SI Appendix*, Fig. S30), including those that promoted self-assembly of the parent peptide, **HEAT_R1**. Notably, a segment of the 1LRV structure corresponding to 2 successive repeat units, $^{123\text{-}170}$1LRV, could be superimposed onto the backbone of 2 adjacent protomers in the **LRV_M3Δ1** peptide with the an RMSD of circa 1 Å for 37 residues of 46 residues, despite the fact that the synthetic helical assembly is left-handed and the native protein is right-handed (Fig. 5). In contrast, significant structural deviations occurred when a similar operation was attempted for the **HEAT_R1** assembly. The structure of one of the protomers with the dimeric asymmetric unit of the **HEAT_R1** filament differed significantly from the structure of the repeat units in 3LTJ (*SI Appendix*, Fig. S16). The structural distortion that would result from packing of a covalently linked **HEAT_dimer** peptide into the **HEAT_R1** filament may preclude self-assembly of the corresponding structure despite the fact that local structural interactions observed in the TRP are conserved.

TRPs do not normally assemble into tubular filaments (vide supra). Indeed, the cohesive interactions are directed solely along the lateral interfaces between repeat motifs with minimal contact along a hypothetical axial interface. This situation closely corresponds to that of helical protein-based polymers, e.g., RecA, Rad51, or OmcS, in which all connectivity in the filament is along the one-start helix (55–57). Coalescence of a helical assembly into a closed nanotube requires formation of axial contacts, which can potentially induce changes in helical symmetry, as in the **LRV_M3Δ1** filament, or even changes in lateral interactions that abrogate conserved structural interactions in the parent repeat protein, as in the **HEAT_R1** filament. We have previously demonstrated that very small local changes in packing can lead to large differences in the quaternary structure for synthetic helical assemblies (18). These structural variations would be challenging to predict from first principles since the energy differences between isoforms may be quite small, which contributes to the common observation of structural polymorphism for peptide and protein filaments assembled in vitro. Helical nanotube formation places more stringent structural requirements on the assembly as stable axial and lateral interfaces must form to initiate and preserve tube formation. If the peptide subunits cannot accommodate these axial interactions, the helical nanotubes may not form or may transition to an alternative structural isoform. Clearly, the latter situation arises with the **HEAT_dimer** peptide, which cannot be accommodated without attendant structural distortion due to symmetry breaking within the filament structure of **HEAT_R1**. In contrast, the **LRV_dimer** peptide can be more easily accommodated into the corresponding filament structure without significant structural distortion.

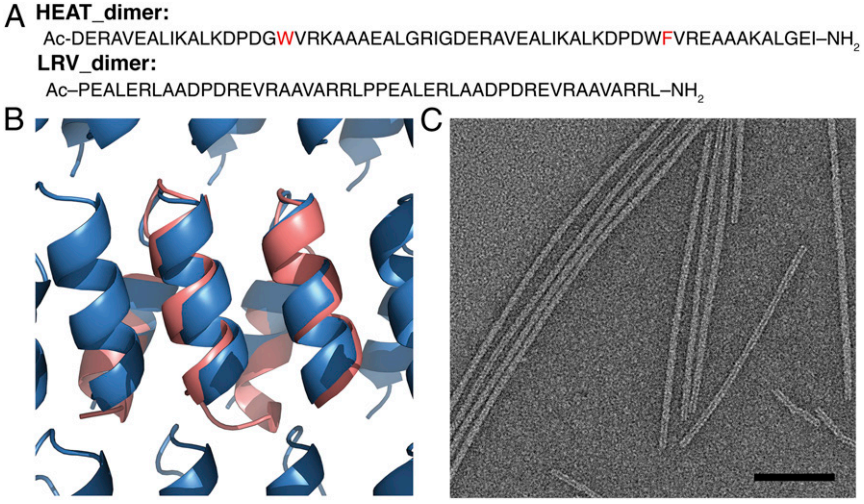

Fig. 5. (*A*) Sequences of the **HEAT_dimer** and **LRV_dimer** peptides. For **HEAT_dimer**, aromatic residues involved in the interprotomer interaction are highlighted in red. (*B*) Backbone overlay of a segment of 1LRV structure (orange), $^{123\text{-}170}$1LRV, corresponding to 2 consecutive repeat units onto the structure of the **LRV_M3Δ1** filament (blue). The view is facing the interior (concave) interface of the filament. The backbone overlay was generated in PyMOL using the extra_fit command. (*C*) TEM image of assemblies of the **LRV_dimer** peptide. (Scale bar, 100 nm.)

Conclusion

The rich functional properties of biologically derived helical assemblies provide motivation for the de novo design of synthetic analogs, which, unconstrained by evolution, can be designed to perform unique functions under conditions that differ significantly from those of the biological environment. While synthetic helical assemblies have been created using nucleic acids as building blocks (58–60), the primary substrates for de novo design strategies have been synthetic peptides and proteins. These materials offer the opportunity for rational design over a diverse range of structural subunits. Moreover, protein- and peptide-based subunits provide the potential advantage that complex functions can be programmed into the assemblies at the sequence level, which can serve as a mechanism to couple function to assembly state. However, de novo design of synthetic peptide assemblies has several significant challenges that complicate the design of protein-based assemblies. Foremost among these is the apparent infinite continuum of interprotomer interfacial geometries that are possible even for structurally simple protomers. This designability problem is most obvious in the recognition that structural polymorphism is common even among helical assemblies derived from native proteins, especially if assembled in vitro under nonnative conditions (15, 16). Furthermore, the de novo design of synthetic helical assemblies necessarily requires validation of the model through structural determination at near–atomic-level resolution. Currently, few structural models have been generated for helical assemblies of synthetic peptides at near–atomic-level to midlevel resolution (17, 18, 37, 61–69). These structures have often revealed significant differences between the model that served as the basis for the design and the corresponding experimental structure.

The native designability of TRPs suggested that these proteins might represent potential substrates for the construction of synthetic helical nanotubes (70), particularly for repeat motifs in which the lateral packing permitted close axial contact between successive turns of the superhelix. Structural analysis of the helical geometry of the PBS_HEAT and LRV concatemers indicated that close contact of axial adjacent repeat motifs was feasible. We have demonstrated that the synthetic peptides **HEAT_R1** and **LRV_M3Δ1**, which are derived from the consensus sequences of PBS_HEAT and LRV repeat motifs, respectively, do indeed form stable helical nanotubes of distinct and unique helical geometry. The results of the structural analyses of the **HEAT_R1** and **LRV_M3Δ1** filaments suggest that the introduction of complementary interactions between appropriately positioned residues can strengthen the axial interface, while conversely, the absence of these interactions can weaken the interface, especially if alternative structural interactions are energetically accessible within the folding landscape. This knowledge provides opportunities for de novo design of helical nanotubes from TRP motifs through use of methods that permit site-directed introduction of stabilizing interactions at the axial interfaces between subunits. The information obtained from the structures of the **HEAT_R1** and **LRV_M3Δ1** filaments provides a convenient starting point for this type of approach.

Materials and Methods

Peptides were prepared using solid-phase peptide synthesis as the *N*-acetyl, *C*-amide derivatives and purified via reverse-phase HPLC. Filaments were assembled from aqueous buffers and characterized initially using CD spectropolarimetry and conventional TEM. Synchrotron SAXS and STEM measurements on the filaments were performed at Argonne National Laboratory and Brookhaven National Laboratory, respectively. Cryo-EM data were collected on grids imaged on a Titan Krios at 300 keV and recorded with a direct electron detector. Helical reconstruction was performed using the IHRSR algorithm (71) after assignment of helical symmetry. Final resolution was determined from FSC between the maps and the models (72). Detailed experimental procedures are described in *SI Appendix*.

ACKNOWLEDGMENTS. This research was, in part, supported by the National Cancer Institute's National Cryo-EM Facility at the Frederick National Laboratory for Cancer Research under contract HSSN261200800001E. This research used resources of the Advanced Photon Source, a US Department of Energy (DOE) Office of Science User Facility operated for the DOE Office of Science by Argonne National Laboratory under contract DE-AC02-06CH11357. This research used the National Cancer Institute's National Cryo-EM Facility at the Frederick National Laboratory for Cancer Research. The cryo-EM work on the HEAT_R1 filaments was conducted at the Molecular Electron Microscopy Core facility at the University of Virginia, which is supported by the School of Medicine and built with NIH grant G20-RR31199. The Titan Krios within that core was funded by NIH shared instrumentation (SIG) grant S10-RR025067, and the Falcon II direct detector was funded by NIH SIG S10-OD018149. This work was supported by NSF Division of Material Research grant 1533958 (to V.P.C. and E.H.E.).

1. C. Sachse, Single-particle based helical reconstruction—How to make the most of real and Fourier space. *AIM Biophysics* **2**, 219–244 (2015).
2. E. H. Egelman, Three-dimensional reconstruction of helical polymers. *Arch. Biochem. Biophys.* **581**, 54–58 (2015).
3. Y. A. Wang *et al*., The structure of a filamentous bacteriophage. *J. Mol. Biol.* **361**, 209–215 (2006).
4. H. Wang, J. N. Culver, G. Stubbs, Structure of ribgrass mosaic virus at 2.9 A resolution: Evolution and taxonomy of tobamoviruses. *J. Mol. Biol.* **269**, 769–779 (1997).
5. O. Morag, N. G. Sgourakis, D. Baker, A. Goldbourt, The NMR-Rosetta capsid model of M13 bacteriophage reveals a quadrupled hydrophobic packing epitope. *Proc. Natl. Acad. Sci. U.S.A.* **112**, 971–976 (2015).
6. T. R. D. Costa *et al*., Structure of the bacterial sex F pilus reveals an assembly of a stoichiometric protein-phospholipid complex. *Cell* **166**, 1436–1444.e10 (2016).
7. A. Loquet *et al*., Atomic model of the type III secretion system needle. *Nature* **486**, 276–279 (2012).
8. N. Poweleit *et al*., CryoEM structure of the Methanospirillum hungatei archaellum reveals structural features distinct from the bacterial flagellum and type IV pilus. *Nat. Microbiol.* **2**, 16222 (2016).
9. F. Wang *et al*., A structural model of flagellar filament switching across multiple bacterial species. *Nat. Commun.* **8**, 960 (2017).
10. A. Lu *et al*., Unified polymerization mechanism for the assembly of ASC-dependent inflammasomes. *Cell* **156**, 1193–1206 (2014).
11. M. J. Knight, C. Leettola, M. Gingery, H. Li, J. U. Bowie, A human sterile alpha motif domain polymerizome. *Protein Sci.* **20**, 1697–1706 (2011).
12. E. H. Egelman, D. J. DeRosier, The Fourier transform of actin and other helical systems with cumulative random angular disorder. *Acta Crystallogr. A* **38**, 796–799 (1982).
13. E. H. Egelman, N. Francis, D. J. DeRosier, F-actin is a helix with a random variable twist. *Nature* **298**, 131–135 (1982).
14. Y. A. Wang, X. Yu, C. Yip, N. C. Strynadka, E. H. Egelman, Structural polymorphism in bacterial EspA filaments revealed by cryo-EM and an improved approach to helical reconstruction. *Structure* **14**, 1189–1196 (2006).
15. E. L. Guenther *et al*., Atomic-level evidence for packing and positional amyloid polymorphism by segment from TDP-43 RRM2. *Nat. Struct. Mol. Biol.* **25**, 311–319 (2018).
16. W. Close *et al*., Physical basis of amyloid fibril polymorphism. *Nat. Commun.* **9**, 699 (2018).
17. E. H. Egelman *et al*., Structural plasticity of helical nanotubes based on coiled-coil assemblies. *Structure* **23**, 280–289 (2015).
18. F. DiMaio *et al*., Atomic-accuracy models from 4.5-Å cryo-electron microscopy data with density-guided iterative local refinement. *Nat. Methods* **12**, 361–365 (2015).
19. H. Garcia-Seisdedos, C. Empereur-Mot, N. Elad, E. D. Levy, Proteins evolve on the edge of supramolecular self-assembly. *Nature* **548**, 244–247 (2017).
20. C. Xu *et al*., Rational design of helical nanotubes from self-assembly of coiled-coil lock washers. *J. Am. Chem. Soc.* **135**, 15565–15578 (2013).
21. W. A. Eaton, J. Hofrichter, Sickle cell hemoglobin polymerization. *Adv. Protein Chem.* **40**, 63–279 (1990).
22. W. Zhang *et al*., Heparin-induced tau filaments are polymorphic and differ from those in Alzheimer's and Pick's diseases. *eLife* **8**, e43584 (2019).
23. A. V. Kajava, Tandem repeats in proteins: From sequence to structure. *J. Struct. Biol.* **179**, 279–288 (2012).
24. F. Parmeggiani *et al*., A general computational approach for repeat protein design. *J. Mol. Biol.* **427**, 563–575 (2015).
25. A. Plückthun, Designed ankyrin repeat proteins (DARPins): Binding proteins for research, diagnostics, and therapy. *Annu. Rev. Pharmacol. Toxicol.* **55**, 489–511 (2015).
26. T. Kajander, A. L. Cortajarena, L. Regan, Consensus design as a tool for engineering repeat proteins. *Methods Mol. Biol.* **340**, 151–170 (2006).
27. B. Kobe, A. V. Kajava, When protein folding is simplified to protein coiling: The continuum of solenoid protein structures. *Trends Biochem. Sci.* **25**, 509–515 (2000).
28. A. K. Das, P. W. Cohen, D. Barford, The structure of the tetratricopeptide repeats of protein phosphatase 5: Implications for TPR-mediated protein-protein interactions. *EMBO J.* **17**, 1192–1199 (1998).
29. P. Michaely, D. R. Tomchick, M. Machius, R. G. Anderson, Crystal structure of a 12 ANK repeat stack from human ankyrinR. *EMBO J.* **21**, 6387–6396 (2002).

30. A. H. Huber, W. J. Nelson, W. I. Weis, Three-dimensional structure of the armadillo repeat region of beta-catenin. *Cell* **90**, 871–882 (1997).
31. M. R. Groves, N. Hanlon, P. Turowski, B. A. Hemmings, D. Barford, The structure of the protein phosphatase 2A PR65/A subunit reveals the conformation of its 15 tandemly repeated HEAT motifs. *Cell* **96**, 99–110 (1999).
32. B. Kobe, J. Deisenhofer, Crystal structure of porcine ribonuclease inhibitor, a protein with leucine-rich repeats. *Nature* **366**, 751–756 (1993).
33. S. Rämisch, U. Weininger, J. Martinsson, M. Akke, I. André, Computational design of a leucine-rich repeat protein with a predefined geometry. *Proc. Natl. Acad. Sci. U.S.A.* **111**, 17875–17880 (2014).
34. L. Doyle *et al*., Rational design of α-helical tandem repeat proteins with closed architectures. *Nature* **528**, 585–588 (2015).
35. K. Park *et al*., Control of repeat-protein curvature by computational protein design. *Nat. Struct. Mol. Biol.* **22**, 167–174 (2015).
36. T. J. Brunette *et al*., Exploring the repeat protein universe through computational protein design. *Nature* **528**, 580–584 (2015).
37. H. Shen *et al*., De novo design of self-assembling helical protein filaments. *Science* **362**, 705–709 (2018).
38. J. W. Peters, M. H. Stowell, D. C. Rees, A leucine-rich repeat variant with a novel repetitive protein structural motif. *Nat. Struct. Biol.* **3**, 991–994 (1996).
39. A. Urvoas *et al*., Design, production and molecular structure of a new family of artificial alpha-helicoidal repeat proteins (αRep) based on thermostable HEAT-like repeats. *J. Mol. Biol.* **404**, 307–327 (2010).
40. T. Kajander, A. L. Cortajarena, E. R. Main, S. G. Mochrie, L. Regan, A new folding paradigm for repeat proteins. *J. Am. Chem. Soc.* **127**, 10188–10190 (2005).
41. A. L. Cortajarena, L. Regan, Calorimetric study of a series of designed repeat proteins: Modular structure and modular folding. *Protein Sci.* **20**, 336–340 (2011).
42. T. Aksel, D. Barrick, Direct observation of parallel folding pathways revealed using a symmetric repeat protein system. *Biophys. J.* **107**, 220–232 (2014).
43. E. Krissinel, K. Henrick, Inference of macromolecular assemblies from crystalline state. *J. Mol. Biol.* **372**, 774–797 (2007).
44. M. K. Hospenthal *et al*., Structure of a chaperone-usher pilus reveals the molecular basis of rod uncoiling. *Cell* **164**, 269–278 (2016).
45. C. N. Spaulding *et al*., Functional role of the type 1 pilus rod structure in mediating host-pathogen interactions. *eLife* **7**, e31662 (2018).
46. M. K. Hospenthal *et al*., The cryoelectron microscopy structure of the type 1 chaperone-usher pilus rod. *Structure* **25**, 1829–1838.e4 (2017).
47. M. A. Neves, M. Yeager, R. Abagyan, Unusual arginine formations in protein function and assembly: Rings, strings, and stacks. *J. Phys. Chem. B* **116**, 7006–7013 (2012).
48. I. Kufareva, L. Budagyan, E. Raush, M. Totrov, R. Abagyan, PIER: Protein interface recognition for structural proteomics. *Proteins* **67**, 400–417 (2007).
49. I. S. Moreira, P. A. Fernandes, M. J. Ramos, Hot spots–A review of the protein-protein interface determinant amino-acid residues. *Proteins* **68**, 803–812 (2007).
50. E. Yashima, K. Maeda, H. Iida, Y. Furusho, K. Nagai, Helical polymers: Synthesis, structures, and functions. *Chem. Rev.* **109**, 6102–6211 (2009).
51. J. Clayden, A. Castellanos, J. Solà, G. A. Morris, Quantifying end-to-end conformational communication of chirality through an achiral peptide chain. *Angew. Chem. Int. Ed. Engl.* **48**, 5962–5965 (2009).
52. K. Kamikawa *et al*., Induction of one-handed helical oligo(*p*-benzamide)s by domino effect based on planar-axial-helical chirality relay. *Chem. Commun. (Camb.)*, 1201–1203 (2009).
53. C. Dolain, H. Jiang, J. M. Léger, P. Guionneau, I. Huc, Chiral induction in quinoline-derived oligoamide foldamers: Assignment of helical handedness and role of steric effects. *J. Am. Chem. Soc.* **127**, 12943–12951 (2005).
54. F. Formaggio *et al*., The first water-soluble 3(10)-helical peptides. *Chemistry* **6**, 4498–4504 (2000).
55. R. M. Story, I. T. Weber, T. A. Steitz, The structure of the E. coli recA protein monomer and polymer. *Nature* **355**, 318–325 (1992).
56. J. M. Short *et al*., High-resolution structure of the presynaptic RAD51 filament on single-stranded DNA by electron cryo-microscopy. *Nucleic Acids Res.* **44**, 9017–9030 (2016).
57. F. Wang *et al*., Structure of microbial nanowires reveals stacked hemes that transport electrons over micrometers. *Cell* **177**, 361–369.e10 (2019).
58. B. Ding *et al*., Interconnecting gold islands with DNA origami nanotubes. *Nano Lett.* **10**, 5065–5069 (2010).
59. D. Liu, S. H. Park, J. H. Reif, T. H. LaBean, DNA nanotubes self-assembled from triple-crossover tiles as templates for conductive nanowires. *Proc. Natl. Acad. Sci. U.S.A.* **101**, 717–722 (2004).
60. P. W. Rothemund *et al*., Design and characterization of programmable DNA nanotubes. *J. Am. Chem. Soc.* **126**, 16344–16352 (2004).
61. S. Q. Zhang *et al*., Designed peptides that assemble into cross-α amyloid-like structures. *Nat. Chem. Biol.* **14**, 870–875 (2018).
62. M. Lee *et al*., Zinc-binding structure of a catalytic amyloid from solid-state NMR. *Proc. Natl. Acad. Sci. U.S.A.* **114**, 6191–6196 (2017).
63. K. H. Chen, K. A. Corro, S. P. Le, J. S. Nowick, X-ray crystallographic structure of a giant double-walled peptide nanotube formed by a macrocyclic β-sheet containing $A\beta_{16\text{-}22}$. *J. Am. Chem. Soc.* **139**, 8102–8105 (2017).
64. K. Nagy-Smith *et al*., Molecular, local, and network-level basis for the enhanced stiffness of hydrogel networks formed from coassembled racemic peptides: Predictions from Pauling and Corey. *ACS Cent. Sci.* **3**, 586–597 (2017).
65. K. Nagy-Smith, E. Moore, J. Schneider, R. Tycko, Molecular structure of monomorphic peptide fibrils within a kinetically trapped hydrogel network. *Proc. Natl. Acad. Sci. U.S.A.* **112**, 9816–9821 (2015).
66. A. R. Cormier, X. Pang, M. I. Zimmerman, H. X. Zhou, A. K. Paravastu, Molecular structure of RADA16-I designer self-assembling peptide nanofibers. *ACS Nano* **7**, 7562–7572 (2013).
67. T. Kajander, A. L. Cortajarena, S. Mochrie, L. Regan, Structure and stability of designed TPR protein superhelices: Unusual crystal packing and implications for natural TPR proteins. *Acta Crystallogr. D Biol. Crystallogr.* **63**, 800–811 (2007).
68. T. H. Sharp *et al*., Cryo-transmission electron microscopy structure of a gigadalton peptide fiber of de novo design. *Proc. Natl. Acad. Sci. U.S.A.* **109**, 13266–13271 (2012).
69. N. C. Burgess *et al*., Modular design of self-assembling peptide-based nanotubes. *J. Am. Chem. Soc.* **137**, 10554–10562 (2015).
70. D. Sanchez-deAlcazar, S. H. Mejias, K. Erazo, B. Sot, A. L. Cortajarena, Self-assembly of repeat proteins: Concepts and design of new interfaces. *J. Struct. Biol.* **201**, 118–129 (2018).
71. E. H. Egelman, A robust algorithm for the reconstruction of helical filaments using single-particle methods. *Ultramicroscopy* **85**, 225–234 (2000).
72. P. V. Afonine *et al*., New tools for the analysis and validation of cryo-EM maps and atomic models. *Acta Crystallogr. D Struct. Biol.* **74**, 814–840 (2018).